Cerebral perfusion simulation using realistically generated synthetic trees for healthy and stroke patients

Hans Christian Rundfeldt [a,b], Chang Min Lee [a], Hanyoung Lee [c], Keun-Hwa Jung [d,*], Hyeyeon Chang [e], Hyun Jin Kim [a,*]

[a] Korea Advanced Institute of Science and Technology, Mechanical Engineering, Republic of Korea
[b] Karlsruhe Institute of Technology, Mechanical Engineering, Germany
[c] Chung-ang University, College of Pharmacy, Republic of Korea
[d] Seoul National University Hospital, Department of Neurology, Republic of Korea
[e] Konyang University Hospital, Department of Neurology, Republic of Korea

ABSTRACT

Background and objective: Cerebral vascular diseases are among the most burdensome diseases faced by society. However, investigating the pathophysiology of diseases as well as developing future treatments still relies heavily on expensive in-vivo and in-vitro studies. The generation of realistic, patient-specific models of the cerebrovascular system capable of simulating hemodynamics and perfusion promises the ability to simulate diseased states, therefore accelerating development cycles using in silico studies and opening opportunities for the individual assessment of diseased states, treatment planning, and the prediction of outcomes. By providing a patient-specific, anatomically detailed and validated model of the human cerebral vascular system, we aim to provide the basis for future in silico investigations of the cerebral physiology and pathology.
Methods: In this retrospective study, a processing pipeline for patient-specific quantification of cerebral perfusion was developed and applied to healthy individuals and a stroke patient. Major arteries are segmented from 3T MR angiography data. A synthetic tree generation algorithm titled tissue-growth based optimization (GBO)[1] is used to extend vascular trees beyond the imaging resolution. To investigate the anatomical accuracy of the generated trees, morphological parameters are compared against those of 7 T MRI, 9.4 T MRI, and dissection data. Using the generated vessel model, hemodynamics and perfusion are simulated by solving one-dimensional blood flow equations combined with Darcy flow equations.
Results: Morphological data of three healthy individuals (mean age 47 years $\pm$ 15.9 [SD], 2 female) was analyzed. Bifurcation and physiological characteristics of the synthetically generated vessels are comparable to those of dissection data. The inability of MRI based segmentation to resolve small branches and the small volume investigated cause a mismatch in the comparison to MRI data. Cerebral perfusion was estimated for healthy individuals and a stroke patient. The simulated perfusion is compared against Arterial-Spin-Labeling MRI perfusion data. Good qualitative agreement is found between simulated and measured cerebral blood flow (CBF)[2]. Ischemic regions are predicted well, however ischemia severity is overestimated.
Conclusions: GBO successfully generates detailed cerebral vascular models with realistic morphological parameters. Simulations based on the resulting networks predict perfusion territories and ischemic regions successfully.

1. Introduction

Neuronal and neurovascular diseases such as stroke, cerebral aneurysms, small vessel disease, and neurodegenerative diseases are prevailing diseases among the world's population. Resulting functional impairment increases morbidity and places a burden on society socially and financially. Stroke ranked as the third leading disease in disability (by disability-adjusted life-years) in 2017 [27]. In 2019, 84.2 per

100,000 fatal cases occurred world-wide, about 50% of which were attributed to ischemic stroke [10]. Small vessel disease is assumed to cause up to 25% of strokes and further contribute to dementia progression in 45% of cases [3]. Despite continuous efforts to understand the underlying pathologies, many diseases remain poorly understood. Further, the need for improved treatment methods to counter these diseases and increase the likelihood of a positive outcome after an intervention persists. However, fundamental research and the development of new therapies or pharmaceutics still heavily relies on in vivo and in vitro studies which are costly and may sometimes sacrifice animals. Simulation models of the cerebral vasculature promise an accelerated and simplified alternative to investigate disease mechanisms, develop novel treatment methods, and test therapies in silico.

Previous studies attempted modeling the cerebrovascular system with various level of complexity. The human cerebral vasculature comprises multiple length scales from macroscale arteries down to microscale capillaries. Macro-scale models are used to simulate hemodynamics of the major arteries using one-dimensional approximations of the governing equations [15,21,19,1,32] or detailed three-dimensional computational fluid dynamics studies [31,34]. While these approaches succeed in estimating local hemodynamics and predict brain areas with insufficient blood supply, the exact mechanisms of cerebral perfusion cannot be assessed due to the absence of smaller arterioles and capillaries. Further, the location of ischemic tissue can only be predicted with low spatial specificity. Other authors explicitly modeled voxel-sized volumes of microvasculature informed by ex-vivo data or based on computational optimization algorithms to elucidate the role of the microvasculature in cerebral perfusion [9,43,4,33,26,47,37]. However, only few approaches have been made to close the gap between large arteries and the microvasculature. Some authors make use of porous media models to approximate small vasculature implicitly, coupled to explicit models of major arteries [23,20,16,43,36,4,9,33,24]. Even though the coupled tissue models provide realistic boundary conditions, the insights that can be gained on the pathology of smaller vessels are severely limited. Further, some studies explicitly model vessels from multiple length scales informed by ex vivo data [28,17,22,42]. While obtaining very detailed models, applications are limited by the destructive techniques used. Ii and Shen et al. used tree generation algorithms to extend segmented vessels to the arteriole level with sparse spatial resolution [22,42]. Neither group proceeded to model vessels of the pre-capillary structures nor estimate cerebral blood flow.

Recently, Kim et al. proposed a novel tree generation algorithm called the growth based optimization (GBO) to extend segmented vessels synthetically based on biologically informed optimization principles [24]. Our study utilizes this work to generate patient-specific explicit models of the cerebral vasculature down to the pre-capillary scale. A major objective of this study is to validate the morphological accuracy of the generated vasculature to prove its feasibility for future applications. Major arteries of three healthy and one diseased patients are segmented from angiographies and extended using the GBO algorithm. Morphological parameters including the segment length, length-to-radius ratio, area ratio (AR),[3] and asymmetry ratio (AS)[4] of the healthy individuals are compared to anatomic data acquired by dissection, 7 T MRI and 9.4 T MRI. Good agreement between the generated vasculature and ex-vivo measured anatomical data is found. Further, a perfusion simulation is conducted utilizing the generated smaller vessels by explicitly coupling them to capillary-level blood transport. The use of porous media perfusion models is limited to small pre-capillary and capillary structures, exploiting the isotropic structures of capillaries while retaining important directionality of arteriole structures. Perfusion results obtained by applying the processing pipeline to healthy patients show good qualitative agreement with perfusion data acquired

using Arterial Spin Labeling MRI and demonstrate the capability to predict gray and white matter distributions in healthy patients. Further, the predictive capabilities of the methodology were explored by simulating perfusion of a stroke patient. The autoregulatory response was successfully modeled and ischemic region in the diseased patient is predicted successfully.

2. Materials and methods

2.1. Tree generation algorithm

Cerebral vessel networks for perfusion simulations are generated in the following steps: First, major cerebral arteries are segmented using Simvascular [46]. Centerline points are recorded with the local vessel radius. Smaller vessels missed in the segmentation are constructed using GBO [24]. GBO generates tree structures by defining an initial tissue configuration around outlets and growing tissue and tree structures in succession until the final tissue volume is reached. The latter is obtained by segmenting tissue from T1-weighted images using Freesurfer [39,12, 13,44,11,40,5–7,14]. Processing steps are depicted in Fig. 1.

2.2. Blood flow simulation algorithms

To describe hemodynamics, a steady, one-dimensional approximation of the Navier-Stokes equations is used for the explicitly modeled vessel networks. The equations are applied per vascular segment and between individual segments mass conservation and the continuity of pressure are enforced. Assuming rigid walls, mass conservation and momentum balance per vascular segment are given by:

Mass conversation: $\dfrac{\partial Q}{\partial z} = 0,$ (1)

Momentum conversation: $\dfrac{\partial Q}{\partial t} + \dfrac{\partial}{\partial z}[(1+\delta)\dfrac{Q^2}{S}] + \dfrac{S}{\rho}\dfrac{\partial p}{\partial z} = S \cdot f + N\dfrac{Q}{S}$.   (2)

Q describes flow rate, p pressure, and S cross-sectional area as a function of the axial coordinate. Further, δ determines a flow profile shape dependent parameter and $N = 8\pi\nu$ describes a viscous loss parameter with the kinematic viscosity ν. Blood is assumed as a Newtonian fluid. External forces f may apply. All equations are assembled in a matrix and solved using a LU decomposition.

Additionally, a Darcy model is solved for small vessels which are not explicitly modeled. It relates flow through a porous medium to pressure driving the flow. For a three-dimensional domain Ω with boundary Γ the Darcy velocity with components $v_i = \dfrac{Q_i}{A}$ equals

$$\boldsymbol{v} = -\dfrac{\kappa}{\mu}\nabla p$$ (3)

inside Ω with fluid density ρ. Here, κ is the tissue permeability and μ is the dynamic viscosity of blood. The velocity field satisfies the boundary conditions

$$\nabla \cdot \boldsymbol{v} = \beta_{source}\left(p_{source} - p\right) - \beta_{sink}\left(p - p_{sink}\right) \text{ in } \Omega.$$ (4)

One Darcy compartment is coupled to each outlet of the vessel model. Local tissue pressure p is related to the source pressure corresponding to computed outlet pressure and the sink pressure set to approximate venous pressure by coupling coefficients β_{source} and β_{sink}. Each β_{source} is given by

$$\beta_{source} = \dfrac{TCBF_{WM/GM}}{(p_{source} - p)},$$ (5)

where $TCBF_{WM/GM}$ describes the target perfusion coefficient of the supplied white or gray matter tissue partition and the mean difference between source pressure and tissue pressure is used in the denominator. Finally, perfusion is estimated per tissue volume by solving the Darcy flow model using a stabilized finite element method solved using a generalized minimum residual method. CBF is defined as

---

[3]   Area ratio (AR).
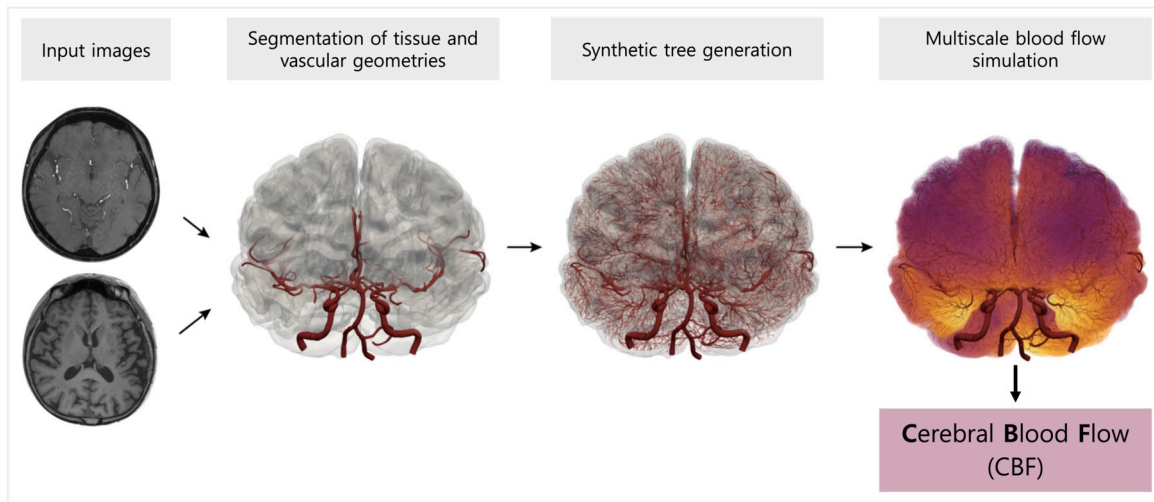[4]   Asymmetry ratio (AS).

Fig. 1. Processing pipeline: from image data to simulated perfusion.

$$CBF = \beta_{sink} \cdot (p - p_{sink}). \tag{6}$$

2.3. Boundary conditions and simulation details

For the one-dimensional blood flow simulations, boundary conditions are assigned at inlets, walls, and outlets of the model. At inlets, mean aortic pressure of 93.3 mmHg is set. Zero flow is set at vessel walls. For each outlet, flow is assigned based on the associated brain tissue volume.

2.4. Autoregulatory mechanism for the cerebrovascular system

An autoregulatory mechanism is applied to approximate cerebral blood flow control mechanisms of the cerebrovascular system. Vasodilation is applied to vessels smaller than a set threshold r_{cutoff} to model vasodilation of arteriole vessels. Due to the pressure-dependent coupling coefficients of the perfusion model, low outlet pressure values are indicative of low perfusion. Hence, outlet pressure values lower than $p_{threshold}$ trigger dilation of the segment and all upstream vessels smaller than r_{cutoff}. Dilation is continued until the pressure rises above $p_{threshold}$ or a maximum dilation $dilation_{max}$ is reached. Pressure and flow are computed initially and computation is repeated following each dilation step until dilation factors converge. Dilation is reported by defining relative change in radius:

$$dilation = \frac{r_{updated} - r_{original}}{r_{original}} \cdot 100 \ [\%]. \tag{7}$$

2.5. Bootstrapping for tree morphology comparison

To validate tree morphology of the generated vasculature, we conducted a comparison study against experimentally obtained tree morphology data. The investigated parameters are shown in Table 1. A direct quantitative comparison between experimental and synthetic data was not feasible due to different sample sizes and resolution of the data. Therefore, synthetic tree data were resampled using bootstrapping. Bootstrapping repetitively executes drawing with replacement from an original sample, creating N resamples with equal number of data points as the compared data. For this, a histogram with 0.05 mm bin-width was created of the radii for all experimental data points. The average radius is used for the segment-specific and the proximal radius for bifurcation-specific data due to data availability. The number of segments per bin of the experimental data are drawn from the equally binned synthetic data randomly and with repetition. Data bins without synthetic data points are excluded from the experimental data. The process is repeated $N = 1000$ times and a synthetic data distribution

with equal number of data points as the experimental distribution is obtained every time. Finally, histograms of the quantities investigated are created from the resampled data and of all the histograms the average is taken per bin. This way, equal numbers of data points and similar radius ranges are included in the experimental and synthetic distributions for fair comparison.

2.6. Scaling of arterial spin labeling data

The ASL data available in this study was acquired at three tesla using a Hadamard sequence. Due to the scanning-time optimized design of this acquisition, a lower signal-to-noise ratio was achieved and the ASL data exhibits physiologically unreasonable perfusion values in some locations. In order to enhance comparability to the simulated results the ASL data was adjusted to match the mean and standard deviation of the simulated perfusion of the whole brain. Further, negative values were set to zero.

2.7. Patient information

This single-center, retrospective study was approved by the local Institutional Review Board (IRB No. H-2204-116-1317). Patients were screened for contraindications to MR before the study and provided informed consent. A T1-weighted image, a TOF-MRA, and a Hadamard-encoded pseudo-continuous ASL were acquired for three healthy and one diseased patients.

3. Results

3.1. Synthetic tree generation

Three healthy individuals (P1, P2, P3[5]; mean age 47 years $\pm$ 15.9 [SD], 2 female) and one diseased patient (PD)[6] were analyzed. Patient characteristics are detailed in Table A.5.

Each tetrahedral element of the finite element volume mesh constructed from the brain tissue corresponds to a tissue partition supplied by one corresponding outlet. Therefore, tissue mesh resolution and tree density are proportional. The vascular networks were generated for two different tissue mesh resolutions resulting in low resolution synthetic tree data (LR) and high resolution synthetic tree data (HR) (Table 2). Only the latter is described in detail.

---

[5] Patient 1 (P1), Patient 2 (P2), Patient 3 (P3).
[6] Patient diseased (PD).

Table 1

Morphology parameters: Quantitative parameters to investigate the vascular morphology.

Parameter	Computation
Geodesic vessel length (L_G)	The geodesic length of a vascular segment connecting two bifurcations.
Average radius (r)	The average radius computed using all discrete points of the segment.
Proximal radius (r_p)	The average radius computed using only the points of the second quartile of the segment.
Distal radius (r_d)	The average radius computed using only the points of the third quartile of the segment.
Length-to-radius-ratio (LR)	The ratio of geodesic vessel length and proximal radius: $LR = \frac{L_G}{r_{proximal}}$.
Area-ratio (AR)	The area ratio of a bifurcation is computed by dividing the area of all children by the parent vessel area using the first and last point respectively where n is the number of children bifurcating from the parent vessel: $AR = \frac{\pi r_1^2 + \ldots + \pi r_n^2}{\pi r_0^2}$.
Asymmetry-ratio (AS)	The asymmetry-ratio is computed by dividing the area of the smallest children vessel of a bifurcation by the area of the largest children: $AS = \frac{\pi r_1^2}{\pi r_2^2} = \frac{r_{child,min}^2}{r_{child,max}^2}$.
Minimum-work-ratio	As proposed by Murray [30], the ratio between parent and children vessels for a binary bifurcation is given as $r_0^3 = r_1^3 + r_2^3$ to comply with the principle of minimum work. To visualize the compliance of the data with this law, a regression between parent and children radii is performed such that $k = \frac{r_1^3 + r_2^3}{r_0^3}$ is obtained.

Table 2

Tree generation results: Quantitative data of vascular trees for low and high resolution.

	Resolution	Number of segments	Number of outlets (WM/GM)	Average outlet size (WM/GM)	Total vascular volume
P1	LR	6353	1559 / 1604	88.34 μm / 135.81 μm	13.1406 cm^3
	HR	221633	39038 / 71765	30.72 μm / 44.48 μm	16.6143 cm^3
P2	LR	6031	1545 / 1471	97.92 μm / 151.40 μm	10.8384 cm^3
	HR	238475	44048 / 75190	30.64 μm / 44.56 μm	14.6183 cm^3
P3	LR	7677	1853 / 1970	94.18 μm / 138.62 μm	13.2215 cm^3
	HR	252873	43700 / 82722	31.70 μm / 45.58 μm	17.3124 cm^3
PD	LR	5314	1254 / 1403	93.21 μm / 147.92 μm	8.68561 cm^3
	HR	200736	35333 / 65035	30.55 μm / 45.20 μm	12.2148 cm^3

Table 3

Tree generation parameters: Parameters used for the generation of synthetic trees.

Parameter	Value
Metabolic work coefficient (m_b)	1×10^7 J/mm^3
Tree data discrete point spacing	0.4 mm
Distance criteria (d)	5.0 cm
Radius-to-flow exponent (k)	3.0
Target perfusion white matter ($TCBF_{WM}$)	20 mL/100 g/min
Target perfusion gray matter ($TCBF_{GM}$)	80 mL/100 g/min

Table 4

Simulation parameters: Parameters used in the perfusion simulation.

Parameter	Value
Source pressure	Computed outlet pressure
Venous pressure	0.0 mmHg
Source conductance (β_{source})	$\frac{TCBF_{WM/GM}}{(p_{source}-p)}$ 1/s/mmHg
Sink conductance (β_{sink})	8.7×10^{-7} 1/s/mmHg
Permeability (κ)	8.0×10^{-8} m^2
Blood viscosity (μ)	0.04 mPa s
Blood density (ρ_{blood})	1.06 g/cm^3
Brain tissue density (ρ_{tissue})	1.05 g/cm^3
Cutoff radius (r_{cutoff})	400 μm
Threshold pressure ($p_{threshold}$)	35 mmHg
Maximum dilation factor (dilation$_{max}$)	50%

Parameter values used for the tree generation and simulation are presented in Table 3 and 4, respectively.
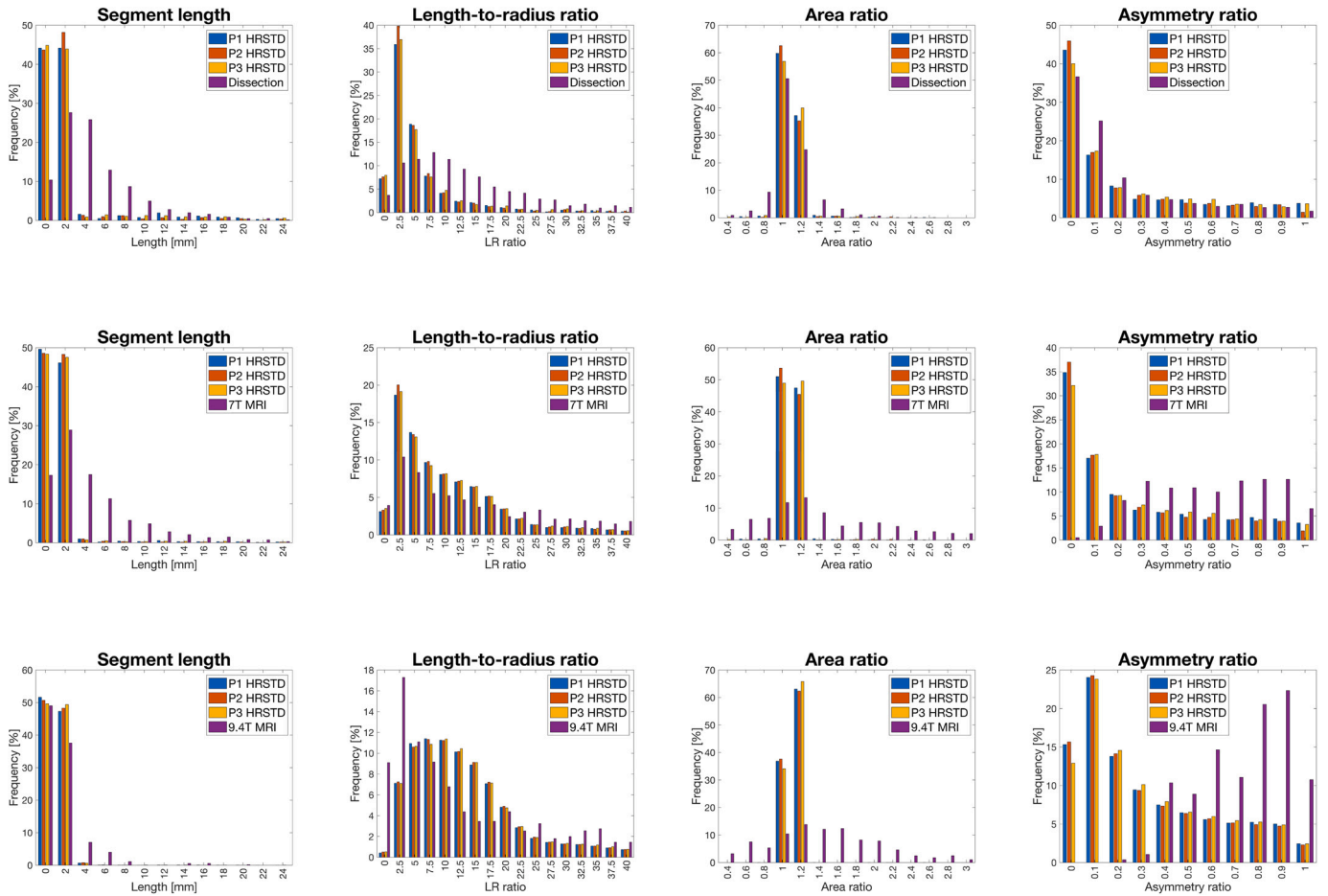
3.2. Tree morphology comparison

Resampled morphological parameters are compared to data obtained by dissection, 7 T MRI, and 9.4 T MRI provided by Helthuis et al. [18] (Fig. 2).

Following the resampling described in section 2.5, synthetic data points with similar radius values as experimental data are selected for comparison to each experimental data set. Hence, synthetic data of each patient varies in the three rows. Synthetic segment lengths exhibit a high number of short segments. Longer segments (larger than 5 mm) are underrepresented in comparison to all experimental data. This happens as the length of vessels generated by the GBO algorithm is dependent on the mesh resolution of the tissue mesh. For the high mesh resolution, short segments are predominantly generated. Morphological parameter comparison with low resolution synthetic tree data are given in the supplements (Fig. A.1). Since similar radius ranges are enforced by the bootstrapping procedure, the distribution of length values translates to the length-to-radius ratios (LR-ratios). Values larger than 25 are underrepresented in synthetic data. Area ratios (AR) show good agreement to dissection data with more than 50% of values between 0.9 and 1.1 in both domains. Small side branches (SSB)[7] bifurcate from larger vessels without significant decrease in area leading to AR's around one. This peak is only observed for dissection data. Larger AR dominate for MRI data as it does not capture SSB appropriately. In 7 T MRI data SSB's remain undetected due to the resolution limitation, resulting in a mismatch in the comparison. In 9.4 T MRI data, only a small volume of microvasculature is investigated. SSB occur on larger vessels and decay towards the pre-capillaries, therefore being underrepresented in the small 9.4 T volume. Only in dissection data SSB's are present, providing a realistic distribution of AR. This observation was made previously by the authors who obtained the experimental data [18] and is confirmed here. Similarly, asymmetry ratios (AS) coincide best with dissection data, where small AS's correspond to SSB's bifurcating from large vessels. Disagreement which is found between the experimental MRI and synthetic data can be attributed to the absence of SSB. Importantly, small SSB in the synthetic tree data are only observed if the resolution of the underlying tissue mesh is sufficiently high to create small vessels. SSB are not resembled well by the low resolution tree data presented in the supplements (Fig. A.1).

---

[7] Small side branch (SSB).

Fig. 2. Morphology comparison: Comparison between three different measured tree morphology parameters and high-resolution synthetic tree data (top row: dissection data, middle row: 7T MRI data, bottom row: 9.4T MRI data). Four different morphological parameters are analyzed: segment length, length-to-radius ratio, area ratio, and asymmetry ratio (left to right).
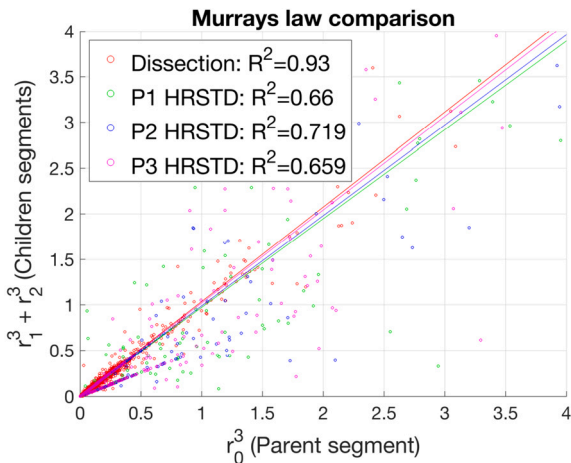
Fig. 3. Minimum work principal: minimum work ratio of healthy patients at high resolution synthetic tree data compared to that of dissection data.

Murray's law postulates that a system of bifurcating tubes utilizes minimal work if bifurcations obey $r_0^3 = r_1^3 + r_2^3$. The linearly regressed relationship is plotted in Fig. 3 in comparison to data obtained using dissection. Robust regression utilizing a bisquare weighting function implemented in the Matlab R2022b *robustfit* function was used to mitigate the effect of outliers. A slope close to one is found for all data sets, indicating the law is obeyed. Smaller vessels coincide better with

the regression while more outliers are present at larger radii which are segmented from medical image data.

3.3. Hemodynamic results of healthy patients

Pressure and flow were simulated for the three healthy subjects. The pressure reduces from the aortic inlet pressure to outlet pressure values between 65 to 80 mmHg with an average outlet pressure of approximately 68 mmHg at radii of 10 μm (Fig. 4). Pressure reduces predominantly in smaller vessels while large arterioles and small arteries carry flow with realtively little pressure reduction. Outlets located distant from inlets have lower pressure than those proximal to inlets, as visible for P1 and P3 where the cerebellum is supplied by posterior inferior cerebellar arteries bifurcating directly from the vertebral arteries. In the case of P2, no cerebellar arteries are included in the segmentation, hence the cerebellum is supplied by posterior cerebral arteries resulting in decreased pressure.

Mean pressure and flow are plotted against radii including standard deviation in the bottom row. Pressure expresses logarithmic behavior with little pressure loss in larger arterioles and increasing pressure loss towards smaller vessels. The mean pressure standard deviation increases towards the smaller outlets. Mean flow expresses exponential shape with decreasing standard deviation for smaller vessels.

3.4. Hemodynamic results of a diseased patient

Processing was repeated for one diseased patient (PD). The partial occlusion of the left internal carotid artery is approximated by
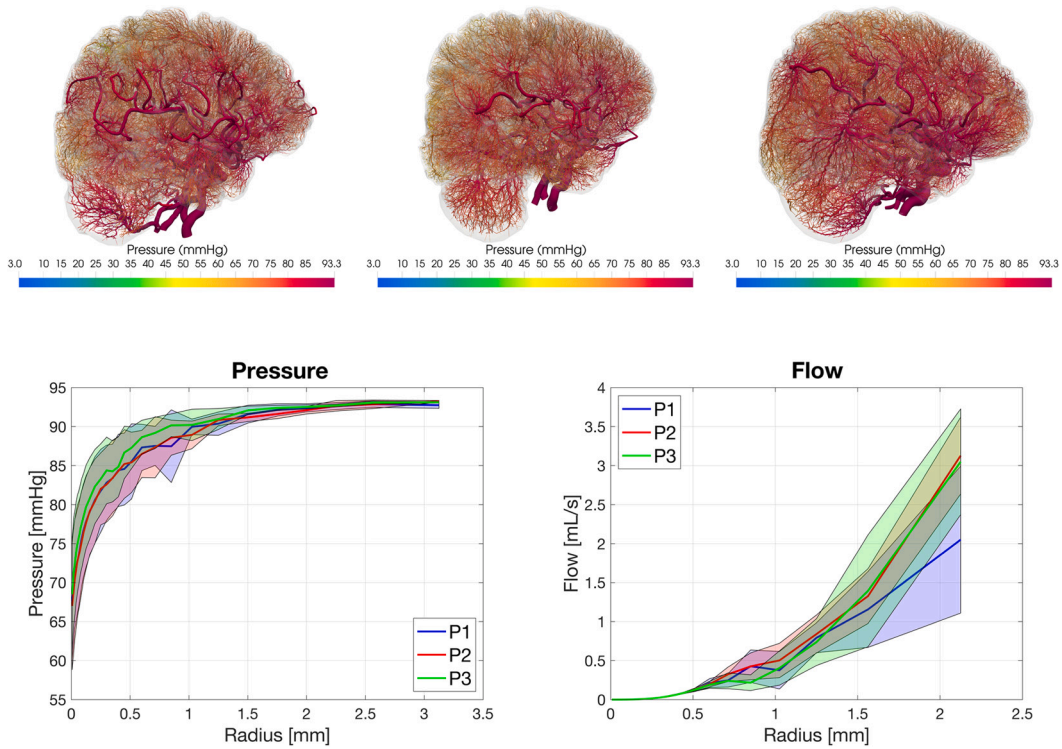
Fig. 4. Pressure and flow distributions: Top row: pressure distribution (P1, P2, P3; left to right). Bottom row: mean pressure and flow with standard deviation over radius values.
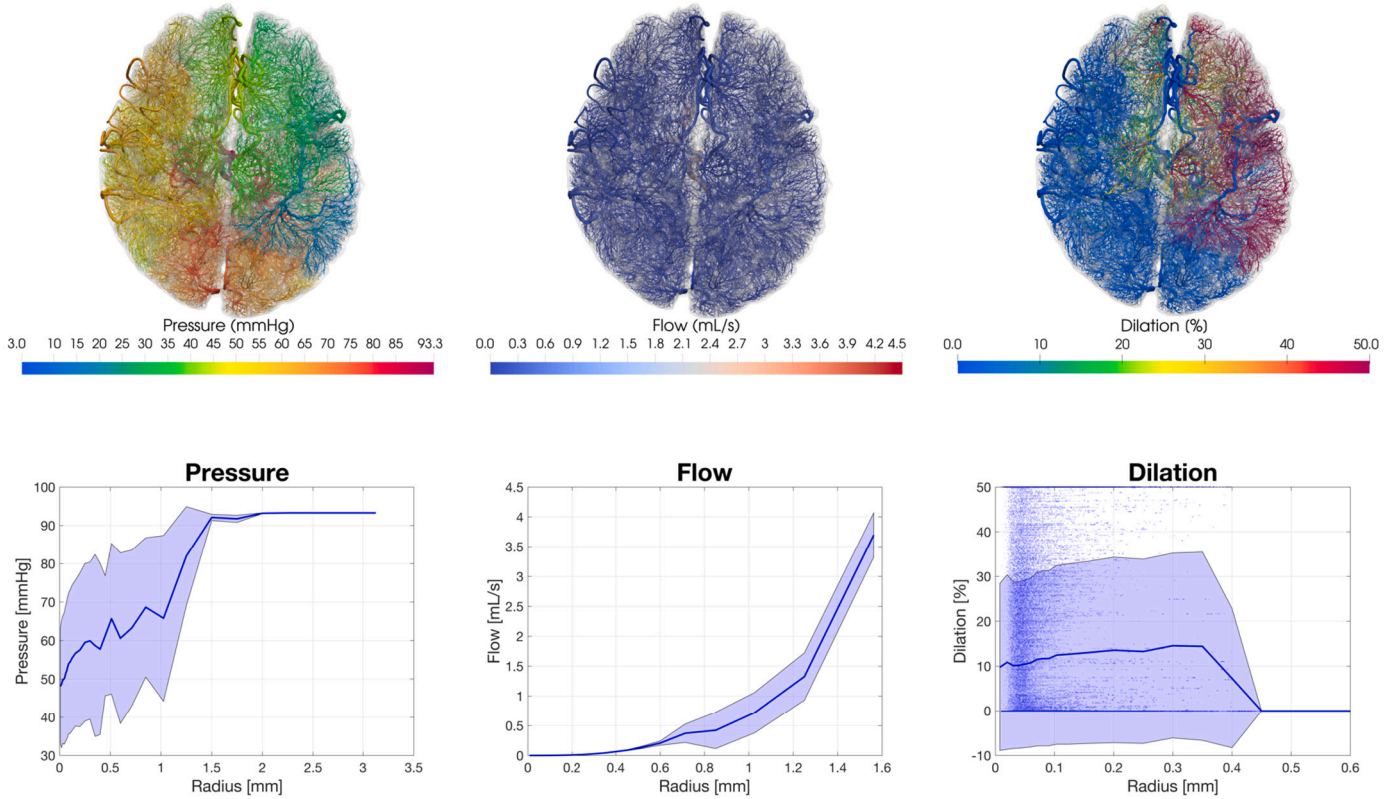

Fig. 5. Pressure, flow, and dilation distributions: Top row: pressure, flow, and dilation distribution for PD. Bottom row: mean pressure, flow, and dilation with standard deviation for PD.

an 80% stenosis causing reduced pressure in the right hemisphere. The stenosis initially causes the simulated pressure gradient between inlets and affected tissue to be insufficient to drive flow to the affected tissue. Although the anterior communicating artery provides a collateral pathway, pressure falls to zero in some areas and flow is diminished. Through vasodilation low pressure is relieved and flow is
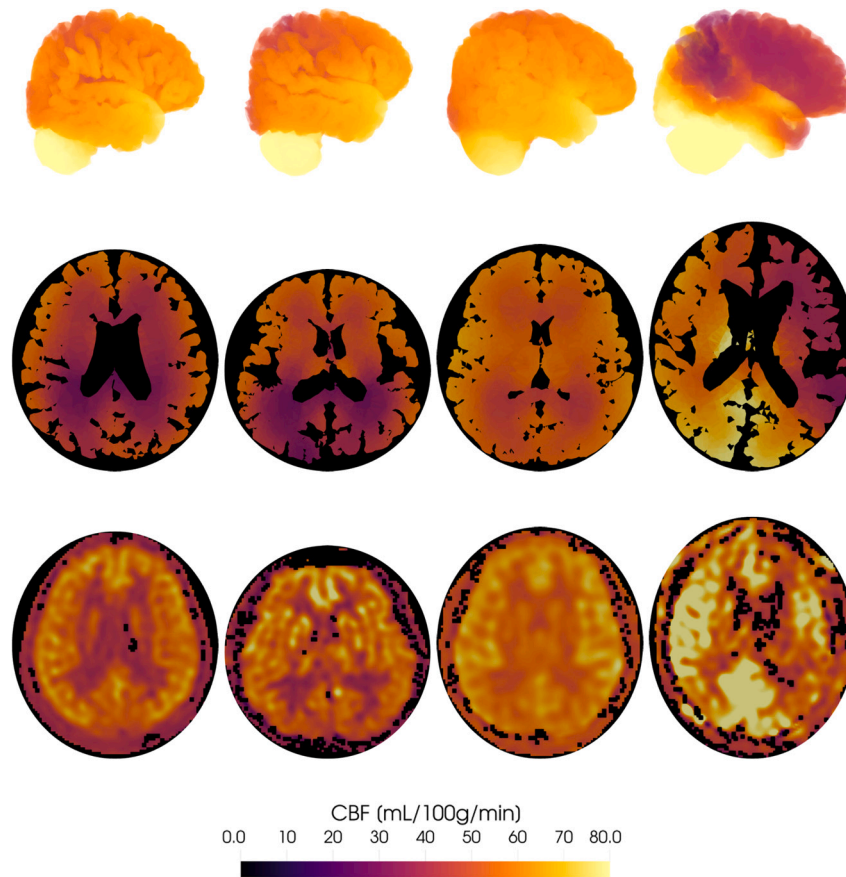
Fig. 6. Perfusion simulation validation: Whole-brain simulated perfusion (top row), simulated perfusion cross-section (middle row, transverse plane), and perfusion estimated by ASL-MRI (bottom row, transverse plane, no contrast) for healthy (P1, P2, P3) and diseased (PD, male, 77 years, right cerebral infarction) patients (left to right).

partially restored proving the capabilities of the autoregulation mechanism. Nevertheless, a maximum dilation of 50% of the original radius is not sufficient to fully relieve ischemia and a region of low pressure persists. Fig. 5 displays the computed pressure, flow, and dilation. When comparing the pressure-radius plot to that of healthy patients, reduced mean pressure, increased pressure oscillations, and increased standard deviation in the range of smaller arterioles are observed. The latter are clearly attributed to the ischemic region. No change to the flow distribution is reported except for the diseased locations. Dilation occurs only for small vessels below the threshold of 400 μm to represent the arteriole vasodilation due to cerebrovascular autoregulation. Maximum dilation is reached almost exclusively in vessels downstream of the diseased vessel. The whole range of possible dilation capacities is utilized with mean dilation around 10%. For the vessels above 350 μm in size, dilation linearly drops to zero.

3.5. Perfusion simulation results

Finally, perfusion is simulated by coupling the vascular model to the Darcy model accounting for small arterioles and capillaries that are omitted in the vascular model. Numerically solving the equations yields the Darcy velocity per tissue partition which is converted to the unit [mL/100 g/min] of cerebral blood flow (CBF). Fig. 6 shows a volume rendering of simulated perfusion for the patients. For healthy patients, simulated CBF is uniform across the brain surface except the cerebellum where high pressure was observed. For the diseased patient, a reduction of CBF values is visible in the diseased region of the right brain hemisphere.

Cross-sections of the brain and a corresponding ASL-acquisition for each individual reveal a symmetric distribution of CBF between both hemispheres for healthy patients. Gray matter areas towards the pial surface and white matter areas located at the cortex center are distinguishable in the simulation and qualitatively match the measured data with good agreement. In the fourth column, results for the diseased patient are displayed. An ischemic region on the right side of the brain corresponding to the occlusion is present. Uneven perfusion is reported for the two brain-hemispheres of the ASL data as well. While the location of ischemia coincides with the location of ASL, there is a mismatch in quantitative values. Simulated ischemia is more severely represented than ischemia recorded by the ASL acquisition.

4. Discussion

We demonstrated the feasibility of the novel tissue-growth-based synthetic tree generation algorithm (GBO) to generate detailed vascular networks. As the GBO algorithm generates synthetic vascular trees efficiently within hours, we generated the networks down to pre-capillary level achieving an unprecedented level of detail.

We compared morphological characteristics against those of measured data and show that the generated synthetic networks are anatomically realistic. We further simulated hemodynamics of blood vessels explicitly down to pre-capillary vessels. We obtained a logarithmic distribution of pressure values against vessel radii which is similar to the findings of Hudetz et al. [21]. For the arterial flow, we obtained an exponential flow distribution against vessel radii. This is confirmed by various in vivo studies that discovered an exponential flow distribution in cat arterioles, rodent arteries, and human retinal vessels [25,38,29]. Recently, Snelling et al. investigated flow in the human cerebrovasculature using phase-contrast MRI and showed qualitative and quantitative agreement with the values observed in this study [41].

Further, we estimated CBF by coupling a perfusion model to the arterial outlets whereby approximating blood flow in the capillary vessels implicitly and compared to perfusion maps measured using medical imaging modalities. Simulated perfusion maps of healthy subjects express distinct areas of gray and white matter. When compared to ASL acquisitions a qualitative match of perfusion areas is observed for healthy patients. However, gradients between gray and white matter areas are less strong in the simulated perfusion maps. This is attributed to a constant pressure-coupling-coefficient assigned at the outlets. As indicated in chapter 2.3, β_{source} values may be updated iteratively to overcome this limitation.

An exponential flow distribution persists for the diseased patient. In areas affected by the occlusion, pressure values are reduced and vessels dilated. These findings comply with observations in patients with carotid artery disease: perfusion pressure decreases and cerebral blood volume increases indicating vessel dilation in some patients [35]. A quantitative mismatch of ischemia between the simulation and ASL acquisition is present showing overestimated under-perfusion in the simulation. However, the predicted location of the ischemia is matched well to that observed in the ASL data. Reasons for the more severe simulated ischemia may be the development of secondary collateral pathways to supply under-perfused tissue. Multiple authors found a significant influence of collateral flow on hemodynamic impairment [2,35]. Further, the effect of autoregulation may be underestimated.

There are limitations in this study. First, this study has investigated three normal subjects and one diseased patient only. While proving the feasibility of the methodology presented, multiple normal and diseased patients with different location and severity of stenosis are to be investigated and a quantitative analysis of the results is needed in the future to assess the applicability of the methods. Second, even though morphological characteristics were realistic when compared against those of the measured data, limitations in the resolution and sample size of the measured data hinder comparability to the synthetic whole-brain vasculature. More through comparison study is needed using segmented vessels of larger volumes acquired by ultra-high-field MRI or modern cone-beam computed tomography [8,45]. Third, the tree generation and perfusion simulation algorithms need to consider collateral networks which are observed frequently in the cerebrovascular system and local adjustment of pressure-coupling-coefficients for more realistic perfusion results. Autoregulation algorithms need to be further improved to better estimate the dilation capacity of patients.

5. Conclusion

The proposed vascular model and the proposed simulation methods have great potential in diagnostic applications, understanding of diseased pathologies, and for in-silico trials of drugs and treatment technologies. Thanks to the computational efficiency of the GBO algorithm unprecedented level of detail with explicit vascular modeling down to the precapillary level was achieved. This level of detail opens the door to other applications next to stroke such as the investigation of small vessel disease and neurodegenerative diseases. By quantifying the morphological accuracy of the vasculature, this study strengthens the applicability for these purposes.

Ethical statement

This single-center, retrospective study was approved by the local Institutional Review Board (IRB No. H-2204-116-1317). Patients were screened for contraindications to MR before the study and provided informed consent.

Declaration of competing interest

The authors have no competing interests to declare that are relevant to the content of this article.

Appendix A. Supplementary material

Supplementary material related to this article can be found online at https://doi.org/10.1016/j.cmpb.2023.107956.

References

[1] J. Alastruey, K.H. Parker, J. Peiró, S.M. Byrd, S.J. Sherwin, Modelling the circle of Willis to assess the effects of anatomical variations and occlusions on cerebral flows, J. Biomech. 40 (2007) 1794–1805, https://doi.org/10.1016/j.jbiomech.2006.07.008.

[2] G.A. Armitage, K.G. Todd, A. Shuaib, I.R. Winship, Laser speckle contrast imaging of collateral blood flow during acute ischemic stroke, J. Cereb. Blood Flow Metab. 30 (8) (2010) 1432–1436, https://doi.org/10.1038/jcbfm.2010.73.

[3] R.J. Cannistraro, M. Badi, B.H. Eidelman, D.W. Dickson, E.H. Middlebrooks, J.F. Meschia, Cns small vessel disease: a clinical review, Neurology 92 (24) (2019) 1146–1156, https://doi.org/10.1212/wnl.0000000000007654.

[4] F. Cassot, F. Lauwers, C. Fouard, S. Prohaska, V. Lauwers-Cances, A novel three-dimensional computer-assisted method for a quantitative study of microvascular networks of the human cerebral cortex, Microcirculation 13 (1) (2006) 1–18, https://doi.org/10.1080/10739680500383407.

[5] A. Dale, B. Fischl, M.I. Sereno, Cortical surface-based analysis: I. Segmentation and surface reconstruction, NeuroImage 9 (2) (1999) 179–194, https://doi.org/10.1006/nimg.1998.0395.

[6] A.M. Dale, M.I. Sereno, Improved localizadon of cortical activity by combining EEG and MEG with MRI cortical surface reconstruction: a linear approach, J. Cogn. Neurosci. 5 (2) (1993) 162–176, https://doi.org/10.1162/jocn.1993.5.2.162.

[7] R.S. Desikan, F. Ségonne, B. Fischl, B.T. Quinn, B.C. Dickerson, D. Blacker, R.L. Buckner, A.M. Dale, R.P. Maguire, B.T. Hyman, M.S. Albert, R.J. Killiany, An automated labeling system for subdividing the human cerebral cortex on mri scans into gyral based regions of interest, NeuroImage 31 (3) (2006) 968–980, https://doi.org/10.1016/j.neuroimage.2006.01.021.

[8] T. Dobrocky, E.I. Piechowiak, J. Goldberg, E.B. Aleman, P. Nicholson, J. Lynch, D. Bervini, J. Kaesmacher, R. Agid, T. Krings, et al., Absence of pontine perforators in vertebrobasilar dolichoectasia on ultra-high resolution cone-beam computed tomography, J. NeuroInterv. Surg. 13 (6) (2021) 580–584, https://doi.org/10.1136/neurintsurg-2020-016818.

[9] W.K. El-Bouri, S.J. Payne, Investigating the effects of a penetrating vessel occlusion with a multi-scale microvasculature model of the human cerebral cortex, NeuroImage 172 (2018) 94–106, https://doi.org/10.1016/j.neuroimage.2018.01.049.

[10] V.L. Feigin, B.A. Stark, C.O. Johnson, G.A. Roth, C. Bisignano, G.G. Abady, M. Abbasifard, M. Abbasi-Kangevari, F. Abd-Allah, V. Abedi, et al., Global, regional, and national burden of stroke and its risk factors, 1990–2019: a systematic analysis for the global burden of disease study 2019, Lancet Neurol. 20 (10) (2021) 795–820, https://doi.org/10.1016/s1474-4422(21)00252-0.

[11] B. Fischl, A. Liu, A.M. Dale, Automated manifold surgery: constructing geometrically accurate and topologically correct models of the human cerebral cortex, IEEE Med. Imaging 20 (1) (2001) 70–80, https://doi.org/10.1109/42.906426.

[12] B. Fischl, D.H. Salat, E. Busa, M. Albert, M. Dieterich, C. Haselgrove, A. van der Kouwe, R. Killiany, D. Kennedy, S. Klaveness, A. Montillo, N. Makris, B.R.A.M. Dale, Whole brain segmentation: automated labeling of neuroanatomicalstructures in the human brain, Neurotechnique 33 (2002) 341, https://doi.org/10.1016/s0896-6273(02)00569-x.

[13] B. Fischl, D.H. Salat, A.J. van der Kouwe, N. Makris, F. Ségonne, B.T. Quinn, A.M. Dale, Sequence-independent segmentation of magnetic resonance images, NeuroImage 23 (2004) S69–S84, https://doi.org/10.1016/j.neuroimage.2004.07.016.

[14] B. Fischl, A. van der Kouwe, C. Destrieux, E. Halgren, F. Ségonne, D.H. Salat, E. Busa, L.J. Seidman, J. Goldstein, D. Kennedy, V. Caviness, N. Makris, B. Rosen, A.M. Dale, Automatically parcellating the human cerebral cortex, Cereb. Cortex 14 (1) (2004) 11–22, https://doi.org/10.1093/cercor/bhg087.

[15] D. Frey, M. Livne, H. Leppin, E.M. Akay, O.U. Aydin, J. Behland, J. Sobesky, P. Vajkoczy, V.I. Madai, A precision medicine framework for personalized simulation of hemodynamics in cerebrovascular disease, Biomed. Eng. Online 20 (1) (2021) 1–20, https://doi.org/10.1186/s12938-021-00880-w.

[16] L. Guo, J.C. Vardakis, T. Lassila, M. Mitolo, N. Ravikumar, D. Chou, M. Lange, A. Sarrami-Foroushani, B.J. Tully, Z.A. Taylor, et al., Subject-specific multi-poroelastic model for exploring the risk factors associated with the early stages of Alzheimer's disease, Interface Focus 8 (1) (2018) 20170019, https://doi.org/10.1098/rsfs.2017.0019.

[17] G. Hartung, S. Badr, S. Mihelic, A. Dunn, X. Cheng, S. Kura, D.A. Boas, D. Kleinfeld, A. Alaraj, A.A. Linninger, Mathematical synthesis of the cortical circulation for the whole mouse brain—Part II: Microcirculatory closure, Microcirculation 28 (2021) 7, https://doi.org/10.1111/micc.12687.

[18] J.H. Helthuis, T.P. van Doormaal, B. Hillen, R.L. Bleys, A.A. Harteveld, J. Hendrikse, A. van der Toorn, M. Brozici, J.J. Zwanenburg, A. van der Zwan, Branching pattern of the cerebral arterial tree, Anat. Rec. 302 (2019) 1434, https://doi.org/10.1002/ar.23994.

[19] J.H. Helthuis, T.P. van Doormaal, S. Amin-Hanjani, X.J. Du, F.T. Charbel, B. Hillen, A. van der Zwan, A patient-specific cerebral blood flow model, J. Biomech. 98 (2020) 109445, https://doi.org/10.1016/J.JBIOMECH.2019.109445.

[20] E. Hodneland, E. Hanson, O. Sævareid, G. Nævdal, A. Lundervold, V. Šoltészová, A.Z. Munthe-Kaas, A. Deistung, J.R. Reichenbach, J.M. Nordbotten, A new framework for assessing subject-specific whole brain circulation and perfusion using mri-based measurements and a multiscale continuous flow model, PLoS Comput. Biol. 15 (2019) 6, https://doi.org/10.1371/journal.pcbi.1007073.

[21] A.G. Hudetz, J.H. Halsey, C.R. Horton, K.A. Conger, D.D. Reneau, Mathematical simulation of cerebral blood flow in focal ischemia, Stroke 13 (1982) 693–700, https://doi.org/10.1161/01.STR.13.5.693.

[22] S. Ii, H. Kitade, S. Ishida, Y. Imai, Y. Watanabe, S. Wada, Multiscale modeling of human cerebrovasculature: a hybrid approach using image-based geometry and a mathematical algorithm, PLoS Comput. Biol. 16 (2020) 6, https://doi.org/10.1371/journal.pcbi.1007943.

[23] T.I. Józsa, R.M. Padmos, N. Samuels, W.K. El-Bouri, A.G. Hoekstra, S.J. Payne, A porous circulation model of the human brain for in silico clinical trials in ischaemic stroke, Interface Focus 11 (2021) 20190127, https://doi.org/10.1098/rsfs.2019.0127.

[24] H.J. Kim, H.C. Rundfeldt, I. Lee, S. Lee, Tissue-growth-based synthetic tree generation and perfusion simulation, Biomech. Model. Mechanobiol. 22 (3) (2023) 1095–1112, https://doi.org/10.1007/s10237-023-01703-8.

[25] M. Kobari, F. Gotoh, Y. Fukuuchi, K. Tanaka, N. Suzuki, D. Uematsu, Blood flow velocity in the pial arteries of cats, with particular reference to the vessel diameter, J. Cereb. Blood Flow Metab. 4 (1) (1984) 110–114, https://doi.org/10.1038/jcbfm.1984.15.

[26] T. Köppl, E. Vidotto, B. Wohlmuth, A 3d-1d coupled blood flow and oxygen transport model to generate microvascular networks, Int. J. Numer. Methods Biomed. Eng. 36 (10) (2020) e3386, https://doi.org/10.1002/cnm.3386.

[27] H.H. Kyu, D. Abate, K.H. Abate, S.M. Abay, C. Abbafati, N. Abbasi, H. Abbastabar, F. Abd-Allah, J. Abdela, A. Abdelalim, et al., Global, regional, and national disability-adjusted life-years (dalys) for 359 diseases and injuries and healthy life expectancy (Hale) for 195 countries and territories, 1990–2017: a systematic analysis for the global burden of disease study 2017, Lancet 392 (10159) (2018) 1859–1922, https://doi.org/10.1016/S0140-6736(18)32335-3.

[28] A. Linninger, G. Hartung, S. Badr, R. Morley, Mathematical synthesis of the cortical circulation for the whole mouse brain-Part I. Theory and image integration, Comput. Biol. Med. 110 (2019) 265, https://doi.org/10.1016/j.compbiomed.2019.05.004.

[29] H.N. Mayrovitz, J. Roy, Microvascular blood flow: evidence indicating a cubic dependence on arteriolar diameter, Am. J. Physiol., Heart Circ. Physiol. 245 (6) (1983) H1031–H1038, https://doi.org/10.1152/ajpheart.1983.245.6.H1031.

[30] C.D. Murray, The physiological principle of minimum work applied to the angle of branching of arteries, J. Gen. Physiol. 9 (6) (1926) 835, https://doi.org/10.1085/jgp.9.6.835.

[31] M. Oshima, R. Torii, S. Tokuda, S. Yamada, A. Koizumi, Patient-specific modeling and multi-scale blood simulation for computational hemodynamic study on the human cerebrovascular system, Curr. Pharm. Biotechnol. 13 (2012) 2153–2165, https://doi.org/10.2174/138920112802502105.

[32] C.S. Park, G. Hartung, A. Alaraj, X. Du, F.T. Charbel, A.A. Linninger, Quantification of blood flow patterns in the cerebral arterial circulation of individual (human) subjects, Int. J. Numer. Methods Biomed. Eng. 36 (2020) 1, https://doi.org/10.1002/cnm.3288.

[33] M. Peyrounette, Y. Davit, M. Quintard, S. Lorthois, Multiscale modelling of blood flow in cerebral microcirculation: details at capillary scale control accuracy at the level of the cortex, PLoS ONE 13 (1) (2018) e0189474, https://doi.org/10.1371/journal.pone.0189474.

[34] A. Polanczyk, M. Podgorski, T. Wozniak, L. Stefanczyk, M. Strzelecki, Computational fluid dynamics as an engineering tool for the reconstruction of hemodynamics after carotid artery stenosis operation: a case study, Medicina 54 (3) (2018) 42, https://doi.org/10.3390/medicina54030042.

[35] W.J. Powers, G.A. Press, R.L. Grubb Jr., M. Gado, M.E. Raichle, The effect of hemodynamically significant carotid artery disease on the hemodynamic status of the cerebral circulation, Ann. Intern. Med. 106 (1) (1987) 27–35, https://doi.org/10.7326/0003-4819-106-1-27.

[36] U.N.A. Qohar, A.Z. Munthe-Kaas, J.M. Nordbotten, E.A. Hanson, A nonlinear multiscale model for blood circulation in a realistic vascular system, R. Soc. Open Sci. 8 (2021) 12, https://doi.org/10.1098/rsos.201949.

[37] J. Reichold, M. Stampanoni, A.L. Keller, A. Buck, P. Jenny, B. Weber, Vascular graph model to simulate the cerebral blood flow in realistic vascular networks, J. Cereb. Blood Flow Metab. 29 (2009) 1429, https://doi.org/10.1038/jcbfm.2009.58.

[38] C.E. Riva, J.E. Grunwald, S.H. Sinclair, B. Petrig, Blood velocity and volumetric flow rate in human retinal vessels, Investig. Ophthalmol. Vis. Sci. 26 (8) (1985) 1124–1132.

[39] F. Segonne, A.M. Dale, E. Busa, M. Glessner, D. Salat, H.K. Hahn, B. Fischl, A hybrid approach to the skull stripping problem in mri, NeuroImage 22 (3) (2004) 1060–1075, https://doi.org/10.1016/j.neuroimage.2004.03.032.

[40] F. Segonne, J. Pacheco, B. Fischl, Geometrically accurate topology-correction of cortical surfaces using nonseparating loops, IEEE Trans. Med. Imaging 26 (2007) 518–529.

[41] R.S. Seymour, Q. Hu, E.S. Snelling, Blood flow rate and wall shear stress in seven major cephalic arteries of humans, J. Anat. 236 (3) (2020) 522–530, https://doi.org/10.1111/joa.13119.

[42] J. Shen, A.H. Faruqi, Y. Jiang, N. Maftoon, Mathematical reconstruction of patient-specific vascular networks based on clinical images and global optimization, IEEE Access 9 (2021) 20648–20661, https://doi.org/10.1109/ACCESS.2021.3052501.

[43] R.J. Shipley, A.F. Smith, P.W. Sweeney, A.R. Pries, T.W. Secomb, A hybrid discrete-continuum approach for modelling microcirculatory blood flow, Math. Med. Biol. 37 (2020) 40, https://doi.org/10.1093/imammb/dqz006.

[44] J. Sled, A. Zijdenbos, A. Evans, A nonparametric method for automatic correction of intensity nonuniformity in mri data, IEEE Trans. Med. Imaging 17 (1998) 87–97, https://doi.org/10.1109/42.668698.

[45] F. Ståhl, H. Almqvist, H. Kolloch, Å. Aspelin, V. Gontu, E. Hummel, M. van Vlimmeren, M. Simon, A. Thran, Å. Holmberg, et al., Dual-layer detector cone-beam ct angiography for stroke assessment: first-in-human results (the next generation x-ray imaging system trial), Am. J. Neuroradiol. 44 (5) (2023) 523–529, https://doi.org/10.3174/ajnr.A7835.

[46] A. Updegrove, N.M. Wilson, J. Merkow, H. Lan, A.L. Marsden, S.C. Shadden, Simvascular: an open source pipeline for cardiovascular simulation, Ann. Biomed. Eng. 45 (2017) 525, https://doi.org/10.1007/s10439-016-1762-8.

[47] N.M. Vaičaitis, B.J. Sweetman, A.A. Linninger, A computational model of cerebral vasculature, brain tissue, and cerebrospinal fluid, Comput.-Aided Chem. Eng. 29 (2011) 1530–1534, https://doi.org/10.1016/B978-0-444-54298-4.50085-4, Elsevier.